RSC Advances

ROYAL SOCIETY OF CHEMISTRY

PAPER

View Article Online
View Journal | View Issue

Cite this: *RSC Adv.*, 2025, **15**, 46981

Photodecarbonylation of π-extended flavonol: mechanistic insights for PDT

Phorntep Promma,[a] Charoensak Lao-Ngam,[b] Pannipa Panajapo,[c] Siramol Photiganit,[c] Ananda Thongyu[c] and Kritsana Sagarik*[c]

Received 14th October 2025
Accepted 13th November 2025

DOI: 10.1039/d5ra07859h

rsc.li/rsc-advances

Photodynamic therapy (PDT) is a promising cancer treatment strategy, with efficacy strongly dependent on the photophysical properties and delivery of the photosensitizer. Photoactivatable carbon monoxide-releasing molecules (photoCORMs) represent a novel class of agents that enable controlled CO release, combining cytotoxic and regulatory effects in cancer cells. In this study, complementary theoretical methods were employed to elucidate the photodecarbonylation mechanism of Flavonol-1 (3-hydroxy-2-phenyl-4*H*-benzo[*g*]chromen-4-one), an organic photoCORM with potential as a dual-function photosensitizer. The DFT and TD-DFT/B3LYP/def2-TZVP approaches were benchmarked against reported photophysical data and applied to model reactions in both low- and high-dielectric environments. For the first time, double excited-state intramolecular proton transfers (ESIPTs) in the S_1 state were shown to drive key acid–base reactions, with solvent polarity critically influencing the competition between fluorescence decay and intersystem crossing (ISC). In nonpolar media, low-barrier ESIPTs favor ISC, whereas in polar solvents, fluorescence of the basic form predominates, consistent with time-resolved spectroscopy. Kinetic and thermodynamic analyses revealed that aerobic pathways leading to salicylic acid ester and CO release are barrierless and energetically favorable, explaining their higher chemical yields compared to the anaerobic pathway producing lactone and CO. Crucially, intersection structures at S_1/T_1, S_1/S_0, and T_1/S_0 crossings were identified as reactive precursors facilitating $^1O_2$ sensitization and CO release *via* rapid ISC. NVE-MDSH simulations estimated that irradiation of Flavonol-1 in an MCF-7 breast cancer cell model could elevate cytosolic temperature to the threshold for thermal necrosis. These theoretical findings suggest that Flavonol-1 could potentially act as a photosensitizer with implications for combined PDT/PTT applications, though experimental validation is required.

Introduction

Photodynamic therapy (PDT) is a nonchemical-based cancer treatment modality that leverages light-activated photosensitizers to generate cytotoxic species, with lower systemic toxicity than traditional chemotherapy.[1–3] In PDT, a photosensitizer absorbs photons of appropriate energy, transitioning to an excited state and transferring energy to target molecules.[1] Effective photosensitizers for therapeutic applications should exhibit strong absorption coefficients in the near-infrared (NIR) or infrared (IR) region for optimal tissue penetration,[4] low photobleaching quantum yields, high intersystem crossing (ISC) efficiency, and minimum toxicity. Key properties include suitable triplet relaxation energy, high phosphorescence quantum yields, and extended triplet state lifetime.[5]

In singlet oxygen-based PDT,[6] a photosensitizer is activated by light to produce singlet oxygen ($^1O_2$), a highly reactive form of oxygen, and other reactive oxygen species. $^1O_2$ plays a crucial role in PDT, particularly in the destruction of cancer cells, pathogens, and tissue abnormalities. Photodynamic reactions can be divided into two types:[1] (i) Type 1 involves free radicals acting as intermediates, transferring electron energy from the photosensitizer to oxygen derivatives and (ii) Type 2 involves the energy released as a result of the singlet (S_1) → triplet (T_1) and $T_1 \rightarrow S_0$ ISC owing to the instability of the photosensitizer in the excited electronic states (*e.g.*, the S_1 and T_1 states). This energy is transferred to triplet oxygen ($^3O_2$), which generally exists at high concentration in cancer cells. Upon receiving this energy, $^3O_2$ changes to $^1O_2$, which is toxic to cancer cells. Therefore, Type 2 photosensitizer has an indirect therapeutic effect in cancer treatment through the $^3O_2 \rightarrow {}^1O_2$ reaction, causing the cancer cells to eventually die.

---

[a] *Department of Chemical Engineering, Faculty of Engineering, Chulalongkorn University, Bangkok 10330, Thailand*

[b] *Chemistry Program, Faculty of Science and Technology, Nakhon Ratchasima Rajabhat University, Nakhon Ratchasima 30000, Thailand*

[c] *School of Chemistry, Institute of Science, Suranaree University of Technology, Nakhon Ratchasima 30000, Thailand. E-mail: kritsana@sut.ac.th; Fax: (+6681) 8783994; Tel: (+6681) 8783994*

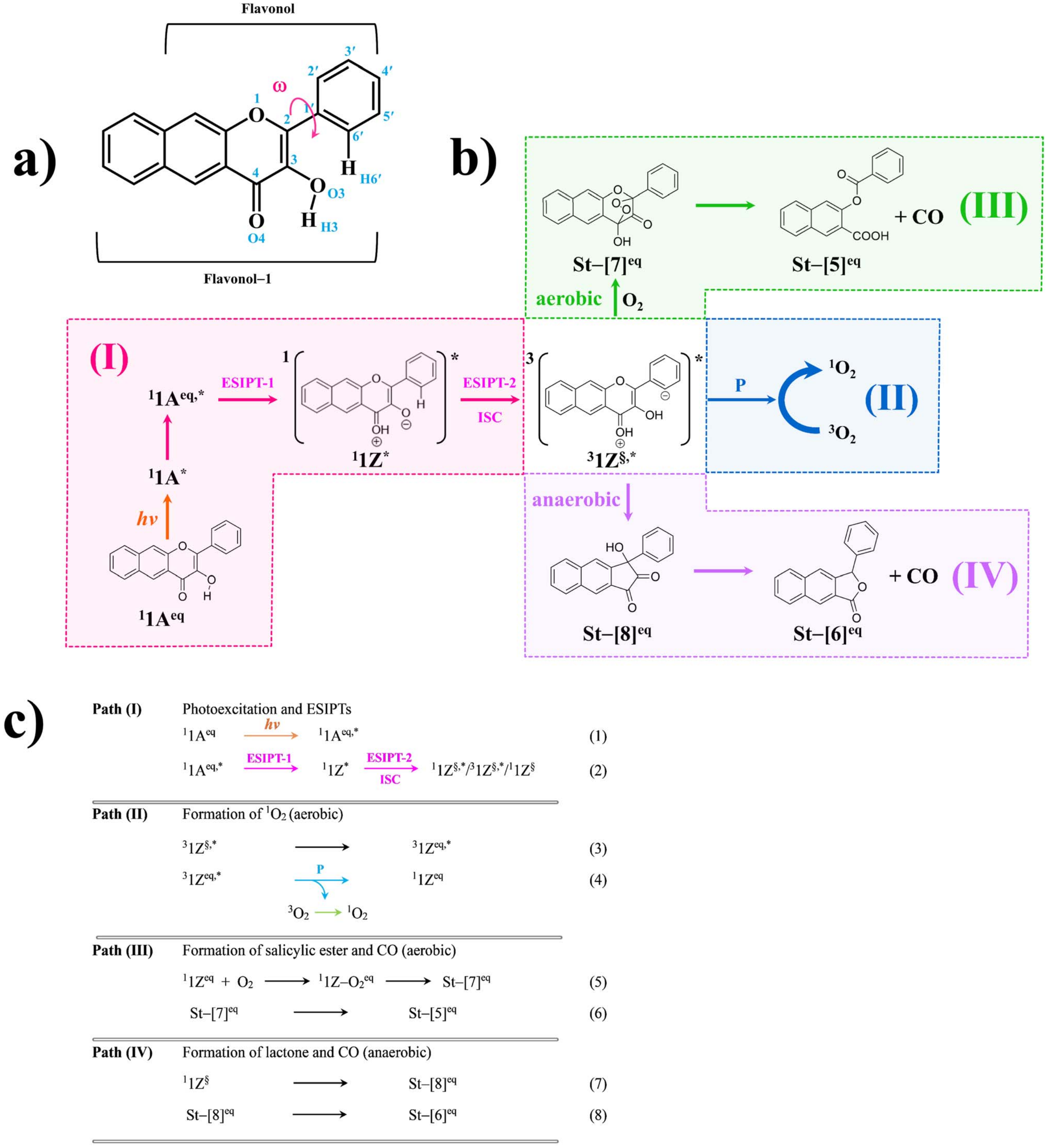

Fig. 1 (a) Structures of Flavonol-1 (3-hydroxy-2-phenyl-4H-benzo[*g*]chromen-4-one) and Flavonol (3-hydroxyflavone) with atom numbering systems. ω = dihedral angle. (b) Proposed mechanism with elementary reactions for the photodecarbonylation of Flavonol-1.[20] (c) Eight elementary reactions proposed based on theoretical results in this study.

The intrinsic toxicity of carbon monoxide (CO) can have therapeutic applications in cancer treatment. CO exposure leads to an antiWarburg effect,[7] which is a metabolic shift in noncancerous stromal cells within the tumor microenvironment, where these cells enhance oxidative phosphorylation and reduce glycolysis. Research has been focused on developing molecules capable of releasing CO [CO-releasing molecules (CORMs)] in cancer cells.[7–11] Photoactivatable CORMs (photo-CORMs) represent a new technology for releasing and managing CO in cancer cells *via* photochemical reactions, controlling CO release in terms of target location and timing.

The release of CO bound to a transition metal complex is one approach through ligand exchange processes, stimulated by solvents or enzymes.[8,10] However, CORMs that bind transition metal complexes tend to have low efficiency in delivering CO to target cancer cells and maintaining the precise release timing. Crucially, metal carbonyl complexes,[7,9,11] initially used as photoCORMs, are adsorbed onto the metal atom after CO release, which might result in unwanted reactions with nearby cells.[12] Thus, transition metal-free photoCORMs (organic photoCORMs) such as cyclopropenones,[13] 1,3-cyclobutadiones,[14] or 1,2-dioxolane-3,4-diones[15] were synthesized, which released CO upon exposure to ultraviolet (UV) radiation. Molecules in this group include cyclic α-diketones[16] and xanthene-containing carboxylic acids.[17,18]

Berreau *et al.*[19] synthesized 3-hydroxy-2-phenyl-4*H*-benzo[*g*]chromen-4-one, an organic photoCORM designated as Flavonol-1 in this study. Flavonol-1 is a π-extended derivative of 3-hydroxyflavone (Flavonol) (**^{1}1A** and **A** presented in Fig. 1a). Flavonol and Flavonol-1 belong to the flavonoid family, which are naturally occurring plant antioxidants with applications in nutrition, pharmaceuticals, and medicine. Flavonoids can act as antioxidants through photochemical reactions by generating CO. Photophysical studies reveal that Flavonol-1 absorbs visible light at longer wavelengths ($\lambda^{\text{abs}} = 344$ and 401 nm (ref. 20) in methanol) with higher quantum yields and CO concentrations than Flavonol ($\lambda^{\text{abs}} = 304$–355 nm in nonpolar solvents).[21] Flavonol has been extensively used as a model molecule in the dynamic and mechanistic studies on excited-state intramolecular proton transfer (ESIPT) in different solvent polarities.[21,22] The ESIPT in 2-methylbutane occurs *via* small-barrier double-well potential, leading to dual fluorescence emissions from the parent molecule (blue) and its proton-transferred tautomer (green).[23]

Several mechanisms have been proposed for CO release from organic photoCORMs under aerobic and anaerobic conditions.[24–27] For Flavonol-1, Russo *et al.*[20] integrated steady-state and transient absorption spectroscopy with quantum chemical calculations to propose a detailed photodecarbonylation pathway in methanol (Fig. 1b), emphasizing ESIPT-driven acid–base reactions as pivotal steps. This study partially adopted the symbols used in ref. 20 to indicate the important chemical species involved in the proposed pathways.

Russo *et al.*[20] suggested that when irradiated with $\lambda^{\text{irr}} = 405$ nm in aerated methanol and degassed solutions, the singlet excited structure **^{1}1A*** tautomerizes to **^{1}1Z*** (a zwitterion-like intermediate) *via* an ultrafast ESIPT [the acid–base reaction in Path (I)], generating **^{3}1Z*** (**^{1}1Z*** in the excited triplet electronic state) *via* ISC. **^{3}1Z*** can be considered as an intermediate for subsequent aerobic and anaerobic pathways (Fig. 1b). The aerobic pathways generate $^1O_2$ [Path (II)], with salicylic ester (**St-[5]$^{\text{eq}}$**) and CO with high chemical yields of 91% and 80%, respectively, in Path (III). Conversely, the anaerobic pathway produces lactone (**St-[6]$^{\text{eq}}$**) and CO with considerably low chemical yields [52–55% in Path (IV)]. The aerobic pathway in Path (II) demonstrates the conversion of $^3O_2 \rightarrow {}^1O_2$, which is toxic to cancer cells (singlet oxygen-based PDT, Type 2).

In our earlier study,[28,29] the photoluminescence mechanism of the BF_2-formazanate dye sensitizers was investigated in the ground (S_0) and excited electronic (S_1 and T_1) states using the density functional theory (DFT) and time-dependent DFT (TD-DFT) methods. The potential energy surface (PES) analysis indicated that the iodinated derivative exhibited a strong tendency to undergo $S_1 \rightarrow T_1$ ISC owing to the heavy atom effect. The transition state theory (TST) calculations showed that this derivative is thermodynamically more stable than the parent compound at room temperature. The theoretical results also confirm that the energy released during the $T_1 \rightarrow S_0$ transition is comparable to the energy required for the $^3O_2 \rightarrow {}^1O_2$ conversion. Moreover, fluorescence and phosphorescence quantum yields might be improved by adjusting the irradiation wavelength and controlling the temperature.

Herein, complementary theoretical methods were used to study the elementary reactions in the proposed photodecarbonylation mechanism of Flavonol-1 (ref. 20) in low (the gas phase with $\varepsilon = 1$) and high (methanol with $\varepsilon = 33$) local dielectric environments. Although methanol is toxic, $\varepsilon = 33$ was selected in this study because most experimental studies were conducted in methanol. The theoretical studies calculated equilibrium structures, energetics, and spectroscopic properties of all chemical species in their S_0, S_1, and T_1 states. The PESs of $S_1 \rightarrow S_0$, $S_1 \rightarrow T_1$, and $T_1 \rightarrow S_0$ transitions were calculated and analyzed based on the double-ended structure method. These PESs were used for analyzing the kinetics and thermodynamics of photodecarbonylation pathways based on the TST. The probability of the internal conversion (IC), ISC, and the effects of solvent polarity on PESs and photophysical properties in S_0, S_1, and T_1 states were explored. To enhance the photodecarbonylation process, this study used nonadiabatic microcanonical molecular dynamics simulations with surface-hopping dynamics (NVE-MDSH). Nonradiative relaxation processes and the impact of molecular dynamics on the IC and ISC were evaluated. The theoretical findings are discussed and compared with available theoretical and experimental data.

Computational methods

Quantum chemical calculations

Herein, the TURBOMOLE 7.80 software package[30] was used for DFT and TD-DFT calculations with the Tamm-Dancoff approximation used within the TD-DFT framework.[31] The Becke, 3-parameter, Lee–Yang–Parr (B3LYP) hybrid functional and valence triple-zeta polarization (def2-TZVP) basis set were used in DFT and TD-DFT calculations based on benchmarking studies relevant to photochemical reactions,[32,33] including those involving boron dipyrromethene (BODIPY)[34] and BF_2-formazanate-based photosensitizers.[29] For glycine photodissociation and formation,[32,33] our benchmark comparisons using the complete active space multiconfigurational second-order perturbation theory (CASPT2) method showed that DFT/B3LYP and TD-DFT/B3LYP provided structural and energetic results on S_0 and S_1 PESs consistent with the CASPT2 method.

The solvent effects on structures and energy were analyzed by incorporating the conductor-like screening model into quantum chemical calculations[35,36] using $\varepsilon = 33$ to represent the methanol solution. All the chemical species involved in the proposed photodecarbonylation mechanism in S_0 were optimized with $\varepsilon = 1$ and 33 using DFT/B3LYP/def2-TZVP, whereas in S_1 and T_1, the

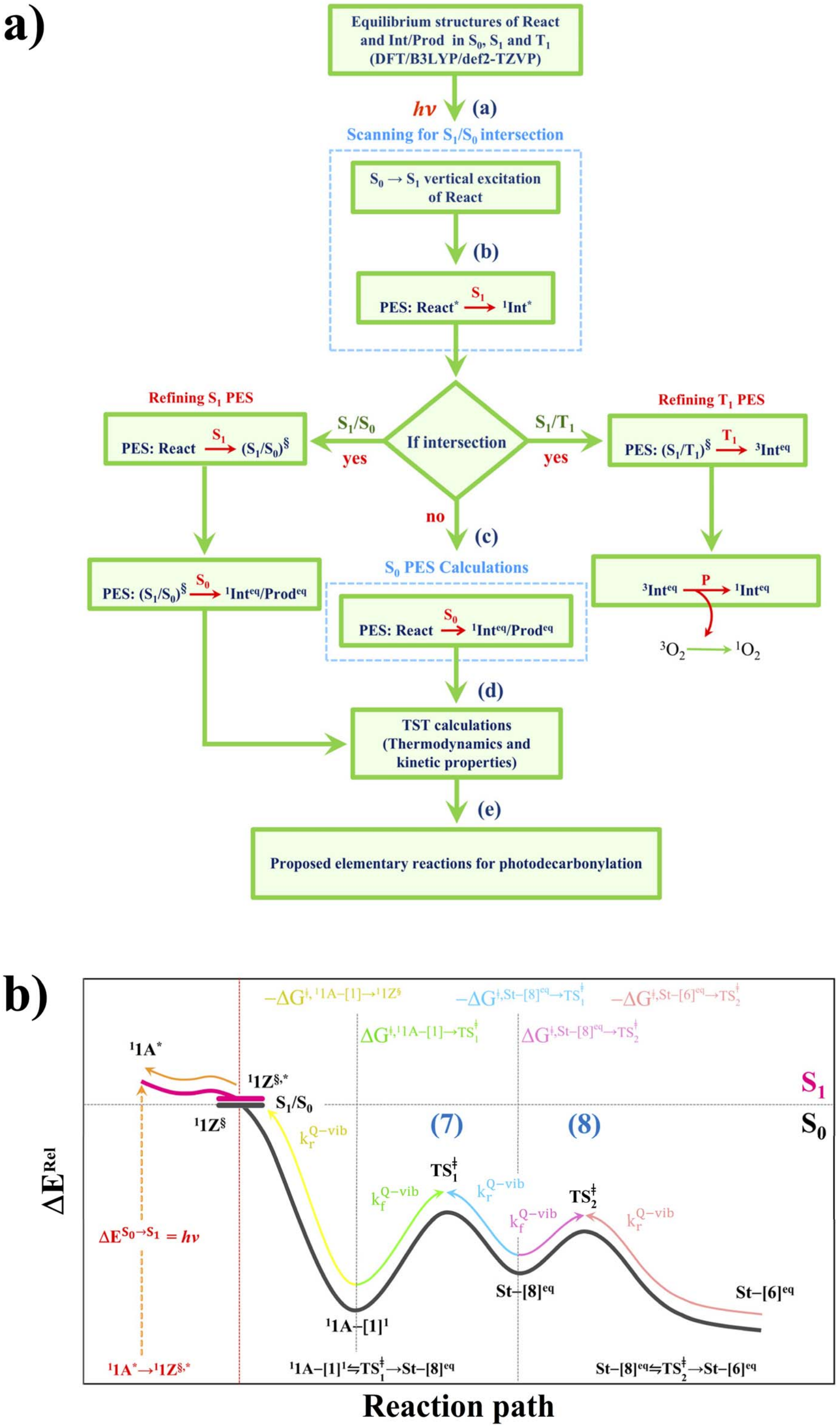

Fig. 2 (a) Theoretical strategies and methods used in the study on the proposed photodecarbonylation mechanism of Flavonol-1 in Fig. 1c. The symbols used are explained in the text. React, Int and Prod = reactant, intermediate and product in elementary reaction, respectively; ^{1} and ^{3} = molecules in singlet and triplet states, respectively. The symbols used are explained in the text. (b) Illustrative diagram used in the calculations of the Gibbs free energies for E(**7**) and E(**8**) in Path (IV) (formation of lactone and CO in E(**7**) and E(**8**)). $\Delta G^{o,E(7)}$ and $\Delta G^{o,E(8)}$ = Gibbs free energies of E(**7**) and E(**8**), respectively; $\Delta G^{o,(IV)}$ = total Gibbs free energies of Path (IV).

equilibrium structures obtained from TD-DFT/B3LYP/def2-TZVP with $\varepsilon = 1$ were used to calculate their energy values with $\varepsilon = 33$. The equilibrium, highest occupied molecular orbital-lowest unoccupied molecular orbital structures, and the total and excitation energy are included in Table S1. The theoretical strategy and methods used in this study are included in Fig. 2a.

Reaction pathway optimization

To systematically study the photodecarbonylation mechanism, the proposed reaction pathways presented in Fig. 1b were primarily explored using the above-mentioned quantum chemical methods. The identified eight elementary reactions [E(**1**)–E(**8**)] are depicted in Fig. 1c. E(**1**) and E(**2**) are photoexcitation and acid–base reactions to generate the intermediate **^{3}1Z*** [Path (I)]. E(**3**)–E(**6**) are aerobic pathways [Paths (II) and (III)], whereas E(**7**) and E(**8**) are the anaerobic pathway [Path (IV)]. To discuss characteristic structures of the chemical species found on the PES, additional character codes were used. The superscripts ($^{\text{eq}}$) and (*) denote the equilibrium and excited structures, respectively, whereas (‡) and (§) represent the transition structure and structure at the S_1/T_1 intersection, respectively. Characteristic structures on the PES are labeled as **St-[*n*]$^{\text{eq}}$** and **St-[*n*]‡**, where *n* is the structure number. **St-[8]$^{\text{eq}}$** and **St-[6]$^{\text{eq}}$** in E(**8**) represent the equilibrium structures on the S_0 PESs. $n =$ **8** and **6** correspond to structures in Fig. 1b.

Because $S_0 \rightarrow T_1$ is spin forbidden, the excited-state PES calculations focused on the reaction occurring on the S_1 PES, which was calculated using the TD-DFT/B3LYP/def2-TZVP method. The $S_0 \rightarrow S_1$ vertical excitation energy ($\Delta E^{S_0 \rightarrow S_1}$) was evaluated, identifying the key structures on S_1 PESs, S_1/S_0 and S_1/T_1 intersections, and $S_1 \rightarrow S_0$, $S_1 \rightarrow T_1$ and $T_1 \rightarrow S_0$ deactivation energy. The structures on S_1 PESs were primarily scanned with $\varepsilon = 1$ using the double-ended structure method,[37,38] which relies on self-consistent PES optimization. Approximately 7–8 structures on PESs were optimized at the TD-DFT/B3LYP/def2-TZVP level of accuracy. The calculations with $\varepsilon = 1$ were performed using the TURBOMOLE 7.80 software package.

To study the effect of the local dielectric environment (solvent polarity) on the excited-state PESs, the structures on S_1 PESs, obtained based on the double-ended structure method with $\varepsilon = 1$, were used in TD-DFT/B3LYP/def2-TZVP calculations with $\varepsilon = 33$. These single-point S_1 PESs with $\varepsilon = 33$ were refined using the nudged elastic band (NEB) method implemented in the ORCA 6.0 software package,[39,40] for which approximately 10 structures along the S_1 PESs were reoptimized with $\varepsilon = 33$ at the same level of accuracy. To verify the TD-DFT/B3LYP/def2-TZVP results with the reported experimental data, the excited-state equilibrium structures and structures at the S_1/S_0 and S_1/T_1 intersections were used in the calculations of fluorescence and phosphorescence wavelengths, and the IC and ISC rates, using the ORCA 6.0 software package.[39,40]

Kinetics and thermodynamics of the reaction pathways

To investigate the kinetics of the rate-determining elementary reactions, quantized vibrational rate constants ($k^{\text{Q-vib}}$) were evaluated over the temperature range of 273–573 K. $k^{\text{Q-vib}}$ was determined using eqn (1),[41] where the zero-point energy-corrected barrier ($\Delta E^{\ddagger,\text{ZPC}}$) was obtained by adding the zero-point correction energy (ΔE^{ZPE}) to the energy barrier ($\Delta E^\ddagger$) on the PES.

$$k^{\text{Q-vib}}(T) = \frac{k_B T}{\hbar} \frac{Q^{\ddagger,\text{ZPC}}}{Q^{\text{R,ZPC}}} e^{-\Delta E^{\ddagger,\text{ZPC}}/k_B T} \tag{1}$$

where $Q^{\text{R,ZPC}}$ and $Q^{\ddagger,\text{ZPC}}$ represent the partition functions of the precursor and transition state structures, respectively, while k_B and $\hbar$ denote the Boltzmann and Planck constants, respectively.

As several elementary reactions in the proposed photodecarbonylation mechanism entail proton/hydrogen transfer, the crossover temperature (T_c) was determined using eqn (2). T_c represents the threshold temperature below which quantum mechanical tunneling predominates in the transition states.[42,43]

$$T_c = \frac{\hbar \Omega^\ddagger}{2\pi k_B} \tag{2}$$

where $\Omega^\ddagger$ is the imaginary frequency of the transition structure. The activation Gibbs free energy ($\Delta G^\ddagger$) was obtained using eqn (3).

$$\Delta G^\ddagger = \left[\ln\left(\frac{k_B T}{\hbar}\right) - \ln k^{\text{Q-vib}}(T)\right] RT \tag{3}$$

The activation enthalpy ($\Delta H^\ddagger$) was calculated using eqn (4).

$$\ln k^{\text{Q-vib}}(T) = \ln A + \frac{\Delta S^\ddagger}{R} - \frac{\Delta H^\ddagger}{RT} \tag{4}$$

$\Delta S^\ddagger$ and R are the activation entropy and gas constant, respectively. $\Delta H^\ddagger$ was determined from the linear correlation between $\ln k^{\text{Q-vib}}$ and $1000/T$.

The important thermodynamic properties were Gibbs free energy (ΔG°) and the equilibrium constants of the elementary reactions ($K^{\text{E}(n)}$). Based on the assumption that the heat released during $S_1 \rightarrow S_0$ (or $T_1 \rightarrow S_0$) is directly transferred to successive elementary reactions in the S_0 state, ΔG° was computed from $\Delta G^\ddagger$, as represented schematically in Fig. 2b [eqn (5)–(7)].

$$\Delta G^{\circ,\text{E}(\mathbf{7})} = \Delta G^{\ddagger,{}^1\mathbf{1A}\text{-}[\mathbf{1}]\rightarrow \text{TS}_1^\ddagger} - \Delta G^{\ddagger,\mathbf{St}\text{-}[\mathbf{8}]^{\mathbf{eq}}\rightarrow \text{TS}_1^\ddagger} \tag{5}$$

$$\Delta G^{\circ,\text{E}(\mathbf{8})} = \Delta G^{\ddagger,\mathbf{St}\text{-}[\mathbf{8}]^{\mathbf{eq}}\rightarrow \text{TS}_2^\ddagger} - \Delta G^{\ddagger,\mathbf{St}\text{-}[\mathbf{6}]^{\mathbf{eq}}\rightarrow \text{TS}_2^\ddagger} \tag{6}$$

$$\Delta G^{\circ,(\text{IV})} = \Delta G^{\circ,\text{El}(\mathbf{7})} + \Delta G^{\circ,\text{El}(\mathbf{8})} \tag{7}$$

Here, $\Delta G^{\circ,\text{E}(7)}$, $\Delta G^{\circ,\text{E}(\mathbf{8})}$, and $\Delta G^{\circ,(\text{IV})}$ are the Gibbs free energies of E(7), E(**8**) and Path (IV), respectively. $K^{\text{El}(n)}$ was calculated from the rate constants in the forward and reverse directions ($k_{\text{f/r}}^{\text{Q-vib}}$). $K^{\text{E}(7)} = k_{\text{f}}^{\text{Q-vib},{}^1\mathbf{1A}\text{-}[\mathbf{1}]\rightarrow \text{TS}_1^\ddagger} / k_{\text{r}}^{\text{Q-vib},\mathbf{St}\text{-}[\mathbf{8}]^{\mathbf{eq}}\rightarrow \text{TS}_1^\ddagger}$ and $K^{\text{E}(\mathbf{8})} = k_{\text{f}}^{\text{Q-vib},\mathbf{St}\text{-}[\mathbf{8}]^{\mathbf{eq}}\rightarrow \text{TS}_2^\ddagger} / k_{\text{r}}^{\text{Q-vib},\mathbf{St}\text{-}[\mathbf{6}]^{\mathbf{eq}}\rightarrow \text{TS}_2^\ddagger}$ for E(7) and E(**8**), respectively. All the kinetic and thermodynamic properties were computed using the DL-FIND program[44] included in the ChemShell software package.[45]

NVE-MDSH simulations

To study the effect of the excitation energy, energy released from nonradiative relaxation processes and the impact of molecular dynamics on deactivation rates, NVE-MDSH simulations were performed in the S_1 state using TD-DFT/B3LYP/def2-TZVP. Based on the Wigner distribution, initial configurations with different $S_0 \rightarrow S_1$ excitation energies were generated and used as starting configurations in NVE-MDSH simulations over time spans of >2.5 ps. Herein, NVE-MDSH simulations were performed using the NEWTON-X[46] interfaced TURBOMOLE 7.80 software package.

In NVE-MDSH simulations, Newton's equations of motion were integrated using the Verlet algorithm with a 0.5 fs time-step. These optimum simulation conditions were validated in our earlier study for examining photochemical reactions.[28] The characteristic structures and dynamics occurring in S_1 and S_0 were classified, and the selected representative NVE-MDSH results were analyzed. To explore the possibility to enhance S_1/S_0 IC, S_1/T_1, and T_1/S_0 ISC, dynamic properties such as intramolecular motion, temperature, and the likelihood of $S_1 \rightarrow S_0$ and $T_1 \rightarrow S_0$ deactivation were emphasized.

Results and discussion

Additional symbols are used to discuss the energies of the characteristic structures on PES: $\Delta E^{S_0 \rightarrow S_1}$ and $\Delta E^{S_1 \rightarrow S_0} = S_0 \rightarrow S_1$ vertical excitation and $S_1 \rightarrow S_0$ relaxation energies, respectively; $\Delta E^{\ddagger}$ = energy barrier on PES; $\Delta E^{S_1/T_1}$ = energy gap between S_1 and T_1 at the intersection. $(\ldots)^{S_0 \rightarrow S_1}$, $(\ldots)^{\ddagger}$, and $(\ldots)^{S_1/T_1}$ are the corresponding energies in the represented figures.

Equilibrium structures

The equilibrium structures of Flavonol-1 obtained from DFT and TD-DFT/B3LYP/def2-TZVP geometry optimizations, energy, and photophysical properties are presented in Table S1. As the results in the gas phase and methanol are not significantly different, the discussion is primarily focused on $\varepsilon = 1$ and the properties with $\varepsilon = 33$ are given in square brackets ([…]). The equilibrium structures of Flavonol-1 in the ground (S_0) and excited electronic (S_1 and T_1) states are slightly different. In S_0, structure $\mathbf{^1A^{eq}}$ (acid form) is characterized by a propeller structure with $\omega = 11°$ [16°] and $\Delta E^{S_0 \rightarrow S_1} = 3.17$ [2.95] eV ($\lambda^{S_0 \rightarrow S_1}$ = 391 [420] nm). The value with $\varepsilon = 1$ is in good agreement with the second outstanding peak obtained in the experiment [ΔE^{ex} = 3.09 eV ($\lambda^{\mathrm{abs}} = 401$ nm)] in methanol.[20]

The equilibrium structure of the intramolecular proton-transferred product of $\mathbf{^1A^{eq}}$ in S_0 is $\mathbf{^1Z^{eq}}$ (base form) (Table S1), characterized by a planar structure [$\angle O_1–C_2–C_{1'}–C_{2'}$ (ω) = $\sim$0°] and $\sim$53 [47] kJ mol^{-1} less stable than $\mathbf{^1A^{eq}}$. The energy is comparable with that obtained using the DFT/B3LYP/TZVP method (50 kJ mol^{-1}).[20] The PES of $\mathbf{^1A^{eq}} \rightarrow \mathbf{^1Z^{eq}}$ isomerization obtained using DFT/B3LYP/def2-TZVP and double-ended structure methods (Fig. S1a) indicates $\Delta E^{\ddagger} = 59.5$ [50.3] and 6.4 [2.9] kJ mol^{-1} in the forward and reverse directions, respectively.

The $\Delta E^{\ddagger}$ for this acid–base reaction is in accordance with the reported experimental findings for Flavonol.[24] The low $\Delta E^{\ddagger}$ for the reverse proton/hydrogen transfer in the ground electronic state of Flavanol, obtained using transient absorption and two-step laser-induced fluorescence, is 3.6 kJ mol^{-1} in *n*-heptane,[24] with the lower rate limit of 60 fs in matrix-isolated argon at 30 K.[47] The TD-DFT/B3LYP/def2-TZVP method yields $\Delta E^{S_0 \rightarrow S_1}$ = 2.49 [2.25] eV ($\lambda^{S_0 \rightarrow S_1} = 498$ [551] nm) for $\mathbf{^1Z^{eq}}$. The theoretical result with $\varepsilon = 1$ is slightly lower than the experimental value in methanol, $\Delta E^{\mathrm{ex}} = 2.62$ eV ($\lambda^{\mathrm{abs}} = 472$ nm).[20]

In the S_1 state, the equilibrium structures $\mathbf{^1A^{eq,*}}$ and $\mathbf{^1Z^{eq,*}}$ are represented by planar structures ($\omega = \sim$0°) with $\Delta E^{S_1 \rightarrow S_0}$ = −2.87 [−2.66] eV ($\lambda^{S_1 \rightarrow S_0} = 432$ [466] nm) and $\Delta E^{S_1 \rightarrow S_0} = -2.31$ [−2.12] eV ($\lambda^{S_1 \rightarrow S_0} = 537$ [585] nm), respectively. The $\lambda^{S_1 \rightarrow S_0}$ of $\mathbf{^1A^{eq,*}}$ with $\varepsilon = 33$ is close to the weak fluorescence ($\lambda_{\mathrm{F}}^{\max} = 472$ nm) observed in the nanosecond time-resolved spectroscopy experiment.[20] The TD-DFT/B3LYP/def2-TZVP results (Table S1) predict the fluorescence rate constants of $\mathbf{^1A^{eq,*}}$ and $\mathbf{^1Z^{eq,*}}$ to be $k_{\mathrm{F}} = 8.58 \times 10^7$ [1.45×10^8] and 9.30×10^7 [1.36×10^8] s^{-1}, respectively. The $\lambda^{S_1 \rightarrow S_0}$ and k_{F} values of $\mathbf{^1Z^{eq,*}}$ calculated with ε = 33 agree with the intense fluorescence band ($\lambda_{\mathrm{F}}^{\max} = 595$ nm) and lifetime ($\tau_{\mathrm{F}} = 5.1 \times 10^{-9}$ s or $k_{\mathrm{F}} = 1/\tau_{\mathrm{F}} = 1.96 \times 10^8$ s^{-1}) measured in methanol.[20]

The equilibrium structure $\mathbf{^3 1Z^{eq,*}}$ in the T_1 state (Table S1) closely resembles $\mathbf{^1Z^{eq,*}}$, with $\Delta E^{T_1 \rightarrow S_0} = -0.79$ [−0.93] eV ($\lambda^{T_1 \rightarrow S_0}$ = 1569 [1333] nm) and the phosphorescence rate constant, $k_{\mathrm{P}} = 1.27 \times 10^1$ [2.14×10^{-1}] s^{-1}. The slow phosphorescence rate of $\mathbf{^3 1Z^{eq,*}}$ supports that Flavonol in the triplet state accounts for the experimentally observed slow reverse proton/hydrogen transfer.[24] These photophysical properties are discussed again in the excited-state PES of Path (II).

Potential energy surfaces

Photoinduced acid–base reaction and singlet-oxygen generation. The S_1 PESs for E(**1**)–E(**4**) with $\varepsilon = 1$ are shown in Fig. 3a–c, with the characteristic structures and energies included in Table S2. To discuss the solvent effect, the energies with $\varepsilon = 33$ were computed using the geometries of S_1 PESs with $\varepsilon = 1$, included in square brackets. When $\varepsilon = 1$, the S_1 PES (Fig. 3a) shows that the $S_0 \rightarrow S_1$ vertically excited structure $\mathbf{^1A^*}$ [E(**1**) in Path (I)] can relax without any $\Delta E^{\ddagger}$ to the equilibrium structure ($\mathbf{^1A^{eq,*}}$) in the S_1 state ($\omega = 0°$).

The S_1 PES (Fig. 3b) suggests a possibility that the rotational (librational) motion of ω in $\mathbf{^1A^{eq,*}}$ (0° < ω < 11°) induces two consecutive ESIPTs with small $\Delta E^{\ddagger}$. The energy barriers for $O_3–H_3 \rightarrow O_4$ and $C_{6'}–H_{6'} \rightarrow O_3$ ESIPTs in $\mathbf{^1Z^*}$ and $\mathbf{^1Z^{\ddagger,*}}$ are $\Delta E^{\ddagger}$ = 6.8 and 9.4 kJ mol^{-1}, respectively. Structure $\mathbf{^1Z^*}$ (the basic form of $\mathbf{^1A^{eq,*}}$) is similar to the Stoke-shifted emitting phototautomer (zwitterionic form) of Flavonol.[20] The PESs (Fig. 3b) also reveal that the consecutive ESIPTs significantly decrease the energy gaps between the electronic states ($\Delta E^{S_1 \rightarrow T_1}$ and $\Delta E^{T_1 \rightarrow S_0}$) and eventually form $\mathbf{^1Z^{\S,*}}$, $\mathbf{^3 1Z^{\S,*}}$, and $\mathbf{^1Z^{\S}}$ at the S_1/T_1 and T_1/S_0 intersections with $k_{\mathrm{ISC}} = 1.40 \times 10^9$ [2.94×10^7] s^{-1} for the S_1/T_1 ISC ($\mathbf{^1Z^{\S,*}} \rightarrow \mathbf{^3 1Z^{\S,*}}$). The fast ISC rates are in good agreement with the experimental results. The femtosecond time-resolved spectroscopy results show $k_{\mathrm{ISC}} = 3.94 \times 10^9$ s^{-1} in methanol.[20]

Based on the hypothesis that the structures at the S_1/T_1 and T_1/S_0 intersections [$\mathbf{^3 1Z^{\S,*}}$ and $\mathbf{^1Z^{\S}}$ in E(**2**)] are the reactive precursors for successive aerobic and anaerobic pathways, several low $\Delta E^{\ddagger}$ deactivation reactions can be suggested from the PES analysis. The PESs (Fig. 3c) reveal that after S_1/T_1 ISC, the $C_{6'} \leftarrow H_{6'}–O_3$ reverse proton/hydrogen transfer occurs and $\mathbf{^3 1Z^{\S,*}}$ can further relax on a barrierless T_1 PES to the

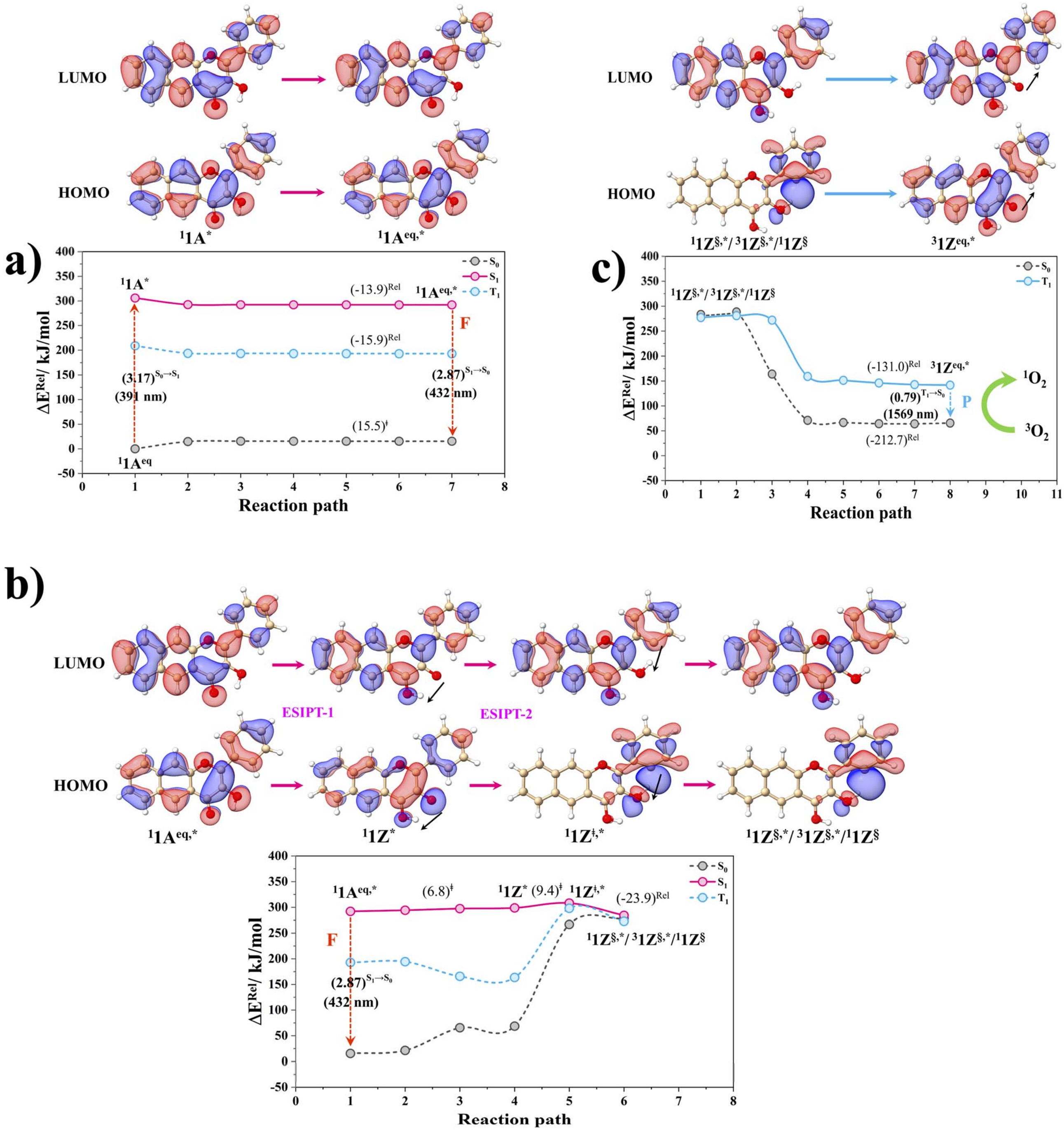

Fig. 3 The PESs for the relaxation of the $S_0 \rightarrow S_1$ vertically excited structure ^{1}**1A*** with $\varepsilon = 1$ obtained from the TD-DFT/def2/TZVP method. The solid lines represent the PESs, whereas the dashed lines denote the PESs calculated using the geometries on the S_1 or T_1 PES. The symbols used are explained in the text. (a) Formation of the equilibrium structure ^{1}**1A**$^{\text{eq},*}$ in the S_1 state *via* ^{1}**1A*** → ^{1}**1A**$^{\text{eq},*}$ [E(**1**) in Fig. 1b]. (b) Formation of the tautomer ^{1}**1Z**§,*, ^{3}**1Z**§,* and ^{1}**1Z**§ at the S_1/T_1 and T_1/S_0 intersections *via* successive ESIPTs and ISC [E(**2**) in Fig. 1b]. (c) The PESs for the relaxation of ^{3}**1Z**§,* at the S_1/T_1 intersection to ^{3}**1Z**$^{\text{eq},*}$ in the T_1 state [E(**3**)] and the $T_1 \rightarrow S_0$ relaxation to transfer energy to the $^3O_2 \rightarrow {}^1O_2$ reaction [E(**4**) in Fig. 1b]. ΔE^{Rel} = relative energy with respect to the precursor in the S_0 state in kJ mol^{-1}; $(\ldots)^{S_0\rightarrow S_1}$, $(\ldots)^{S_1\rightarrow S_0}$ and $(\ldots)^{T_1\rightarrow S_0}$ = excitation and relaxation energies in eV; (…nm) = excitation or relaxation electronic energy in nm; $(\ldots)^{\text{Rel}}$ and $(\ldots)^{\ddagger}$ = relaxation energy and energy barrier on PES in kJ mol^{-1}; → = proton/hydrogen transfer direction.

equilibrium structure in the T_1 state (^{3}**1Z**$^{\text{eq},*}$), followed by the $T_1 \rightarrow S_0$ phosphorescence (P). Because $T_1 \rightarrow S_0$ relaxation energy of ^{3}**1Z**$^{\text{eq},*}$ ($\Delta E^{T_1\rightarrow S_0} = -0.79$ [-0.93] eV) is close to the energy required for experimentally observed $^3O_2 \rightarrow {}^1O_2$ ($\Delta E^{T_1\rightarrow S_0} = 0.97$ eV),[6] the hypothesis that the aerobic pathway to generate $^1O_2$ *via* E(**4**) in Path (II) is validated.

Comparison of the S_1 and T_1 potential energy profiles of E(**1**)–E(**4**) with $\varepsilon = 1$ in Fig. 4 and with $\varepsilon = 33$ in Fig. S1b reveals similar trends of the relative energy, with a considerably higher energy barrier for the second ESIPT ($C_{6'}$–$H_{6'}$ → O_3) with $\varepsilon = 33$ ($\Delta E^{\ddagger} = [83.7]$ kJ mol^{-1}). As S_1 and T_1 energies with $\varepsilon = 33$ (Fig. S1b) were computed using the geometries with $\varepsilon = 1$ (Fig. 4), the single-point S_1 potential energy profile with $\varepsilon = 33$ (Fig. S1b) was verified using the NEB method included in the ORCA 6.0 software package. The S_1 PES with $\varepsilon = 33$ (Fig. S2a) exhibits similar structural and energetic features with a slightly higher energy barrier for the second ESIPT ($\Delta E^{\ddagger} = [91.3]$ kJ mol^{-1}).

The high $\Delta E^{\ddagger}$ confirms that E(**2**) is kinetically more favorable with $\varepsilon = 1$. Because the second ESIPT (^{1}**1Z**$^{\ddagger,*,\varepsilon}$) precedes the S_1/T_1 ISC (Fig. S1b), the high $\Delta E^{\ddagger}$ with $\varepsilon = 33$ can result in an increased likelihood for $S_1 \rightarrow S_0$ fluorescence of ^{1}**1Z**$^{*,\varepsilon}$ ($\lambda^{S_1\rightarrow S_0} = 585$ nm) and decreased likelihood for $T_1 \rightarrow S_0$ relaxation, where the relaxation energy promotes $^3O_2 \rightarrow {}^1O_2$ [Path (II)]. This conjecture is supported by the intense fluorescence band of the basic form (^{1}**1Z**$^{*,\varepsilon}$) observed *via* nanosecond time-resolved spectroscopy ($\lambda_F^{max} = 595$ nm).[20]

The analysis of the photophysical properties (Table S1) suggests that while the phosphorescence rates ($k_P = 1.27 \times 10^1$ [2.14×10^{-1}] s^{-1}) of ^{3}**1Z**^{eq,*} ($T_1 \rightarrow S_0$) are slow, the ^{1}**1Z**$^{\S,*} \rightarrow {}^3$**1Z**§,* ISCs are extremely fast ($k_{ISC} = 1.40 \times 10^9$ [2.94×10^7] s^{-1}). These findings confirm the potential application of Flavonol-1 as a photosensitizer in photodynamic therapy (photoCORM);[5] a fast ISC rate with a slow phosphorescence rate are two desirable properties for an effective photosensitizer in photodynamic therapy.

Aerobic decarbonylation pathway. To study E(**5**) and E(**6**) in Path (III) in the aerobic decarbonylation pathway to generate salicylic acid ester and CO (Fig. 1c), the intermediate and product (**St-[7]^{eq}** and **St-[5]^{eq}**; Fig. 1b) were primarily optimized using the DFT/B3LYP/def2-TZVP method. Structure **St-[7]^{eq}** features a peroxide bond bridging C_4 and C_2 atoms and the hydroxyl (O–H) group at the C_4 atom (base form), whereas **St-[5]^{eq}** is represented by the salicylic acid ester interacting with CO through van der Waals interaction, $\Delta E^{vdW} = -1.29$ [4.19] kJ mol^{-1}.

Based on the hypothesis that the structures at S_1/T_1 and T_1/S_0 intersections are the precursors to generate **St-[7]^{eq}** in E(**5**), the equilibrium structure of ^{1}**1Z**§ interacting *via* van der Waals force with an O_2 molecule (^{1}**1Z-O$_2$^{eq}**; Fig. 5a)[24,48] was optimized and used in the PES calculation. The double-ended structure scan (Fig. 5a) shows that ^{1}**1Z-O$_2$^{eq}** → **St-[7]^{eq}** is highly exothermic ($\Delta E^{Rel} = -190.8$ [-188.4] kJ mol^{-1}), which proceeds with a low energy barrier ($\Delta E^{\ddagger} = 5.3$ [3.6] kJ mol^{-1}). Similar results were obtained for the decarbonylation reaction. The **St-[7]^{eq}** → **St-[5]^{eq}** reaction (Fig. 5b) occurs on a barrierless potential with $\Delta E^{Rel} = -394.8$ [-400.0] kJ mol^{-1}. The overall potential energy profiles obtained with $\varepsilon = 1$ and 33 (Fig. 5c) reveal that for the photodecarbonylation on the aerobic pathway [Path (III)], E(**5**) and E(**6**) are kinetically and thermodynamically favorable.

Anerobic decarbonylation pathway. A similar approach was used to study E(**7**) and E(**8**) in Path (IV) for the photodecarbonylation on the anaerobic pathway. After the T_1/S_0 ISC, the S_0 PESs of ^{1}**1Z**§ → **St-[8]^{eq}** (Fig. 6a) show high energy barriers ($\Delta E^{\ddagger} = 116.3$ [105.0] kJ mol^{-1}) for E(**7**). The **St-[8]^{eq}** → **St-[6]^{eq}** decarbonylation to generate lactone and CO (Fig. 1b) possesses lower energy barriers ($\Delta E^{\ddagger} = 37.9$ [43.2] kJ mol^{-1}) for E(**8**) with $\Delta E^{vdW} = -1.94$ [2.36] kJ mol^{-1}. As E(**7**) and E(**8**) were the exclusive rate-determining processes (Fig. 6a and b), the energy barriers obtained based on the double-ended structure method were refined *via* transition state (TS) optimizations. The refined transition states obtained with only one imaginary frequency are ^{1}**1A-[2]**‡ and ^{1}**1Z-[2]**$^{\ddagger,\varepsilon}$ (Fig. 6c), with the energy barrier significantly lower for E(**7**) with $\varepsilon = 33$ ($\Delta E^{\ddagger} = 71.7$ [7.7] kJ mol^{-1}), whereas E(**8**) proceeds on barrierless PESs both in $\varepsilon = 1$ and 33 *via* **St-[9]^{eq}**.

The discrepancies between the energy barriers calculated with $\varepsilon = 1$ and 33 (Fig. 6c) arise because ^{1}**1Z**§ → ^{1}**1A**^{eq} ($\varepsilon = 1$) is characterized by double proton/hydrogen reverse transfers (O_4–H_3 → O_3 and O_3–$H_{6'}$ → $C_{6'}$), whereas ^{1}**1Z**§ → ^{1}**1Z**$^{eq,\varepsilon}$ ($\varepsilon = 33$) is

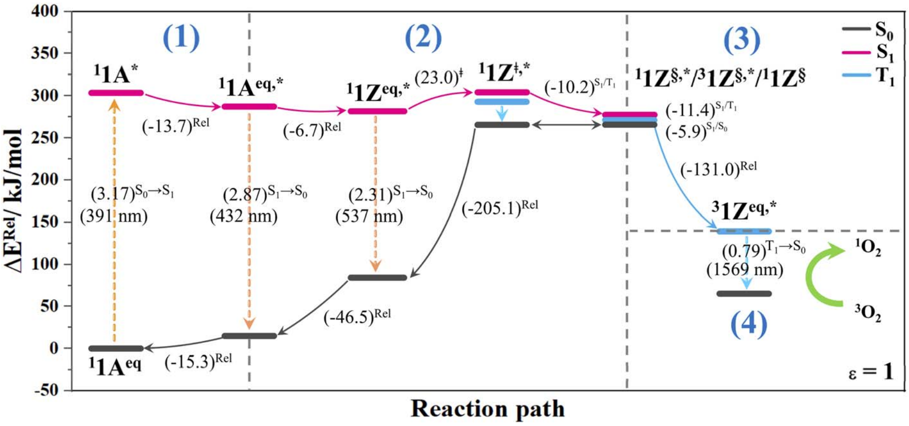

Fig. 4 The S_1, T_1 and S_0 potential energy profiles for the successive ESIPTs [E(**1**)–E(**2**) in Path (I)] and the energy transfer to the $^3O_2 \rightarrow {}^1O_2$ reaction [E(**3**)–E(**4**) in Path (II)] with $\varepsilon = 1$. The solid lines represent the energies obtained from the double-ended structure method in $\varepsilon = 1$. ΔE^{Rel} = relative energy with respect to the precursor in the S_0 state in kJ mol^{-1}; $(\ldots)^{S_0\rightarrow S_1}$, $(\ldots)^{S_1\rightarrow S_0}$ and $(\ldots)^{T_1\rightarrow S_0}$ = excitation and relaxation energies in eV; (…nm) = excitation or relaxation energy in nm; $(\ldots)^{Rel}$ and $(\ldots)^{\ddagger}$ = relative energy and energy barrier on PES; $(\ldots)^{S_1/T_1}$ and $(\ldots)^{T_1/S_0}$ = energy gaps at the intersections of two electronic states in eV.

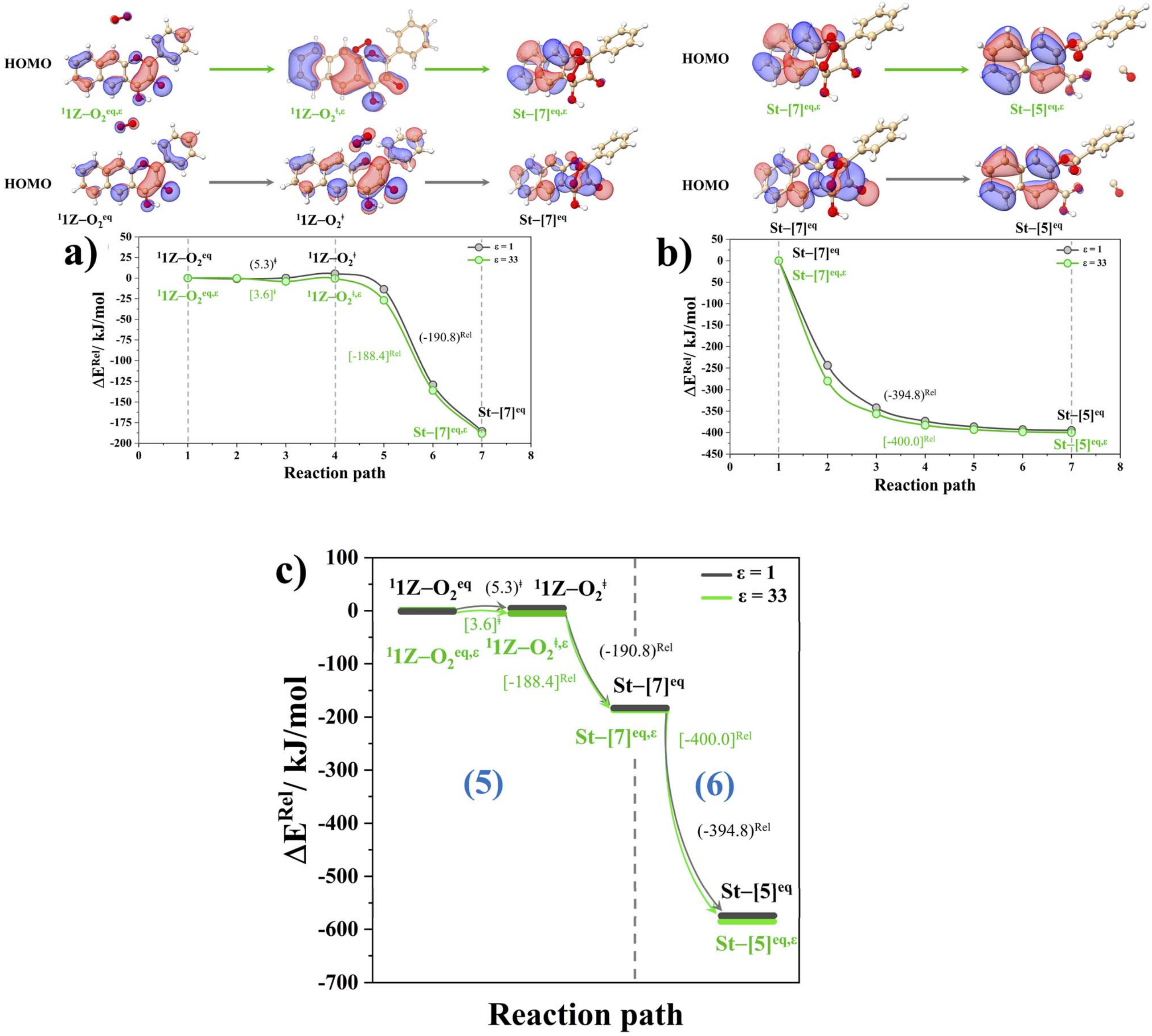

Fig. 5 (a and b) The S_0 PESs for formation of salicylic ester and CO on the aerobic pathway with $\varepsilon = 1$ and 33, E(**5**) and E(**6**) in Path (III), respectively. (c) The S_0 potential energy profiles for formation salicylic ester and CO on the aerobic pathway in the S_0 state [Path (III)]. The symbols used are explained in the text. ΔE^{Rel} = relative energy with respect to the precursor in the S_0 state in kJ mol^{-1}; $(\ldots)^{\mathrm{Rel}}$ and $(\ldots)^{\ddagger}$ = relaxation energy and energy barrier on PES in $\varepsilon = 1$; […] = energy with $\varepsilon = 33$.

represented exclusively by single reverse transfer (O_3–$H_{6'} \rightarrow C_{6'}$), and both lead to six- to five-membered ring contraction (**St-[8]^eq**). Comparison of the potential energy profiles reveals that for photodecarbonylation, the aerobic pathway [Path (III); Fig. 5c] is kinetically and thermodynamically more favorable than the anerobic pathway [Path (IV); Fig. 6c], and the formation of the intermediate **St-[8]^eq** on the anerobic pathway [E(7)] is the only rate-determining reaction.

To further discuss the effect of the solvent polarity, additional S_0 PESs for **^{1}1Z§** → **St-[8]^eq** in different local dielectric environments were computed and compared (Fig. S2b): the gas phase ($\varepsilon = 1$), ethanol ($\varepsilon = 24$), methanol ($\varepsilon = 33$), and aqueous solutions ($\varepsilon = 80$). The adiabatic potential energy profiles (Fig. S2c) illustrate that $\Delta E^{\ddagger}$ vary from 71.7 kJ mol^{-1} to 6.1 kJ mol^{-1} within this range. Because the intracellular (*e.g.*, the cell membrane, cytoplasm medium, and enveloping nucleus) dielectric constants are reported in the range of ~30 and ~60,[49] the $\Delta E^{\ddagger}$ for the intracellular decarbonylation on the anaerobic pathway [Path (IV)] is anticipated to be low (approximately 7.7–6.1 kJ mol^{-1}) as shown in Fig. 6d. A schematic diagram summarizing all the aerobic and anaerobic pathways involved in the photodecarbonylation process is shown in Fig. 7.

Thermodynamics and kinetics of elementary reactions

The kinetics and thermodynamics of elementary reactions were analyzed to suggest general experimental conditions for effective photodecarbonylation. The adiabatic potential energy

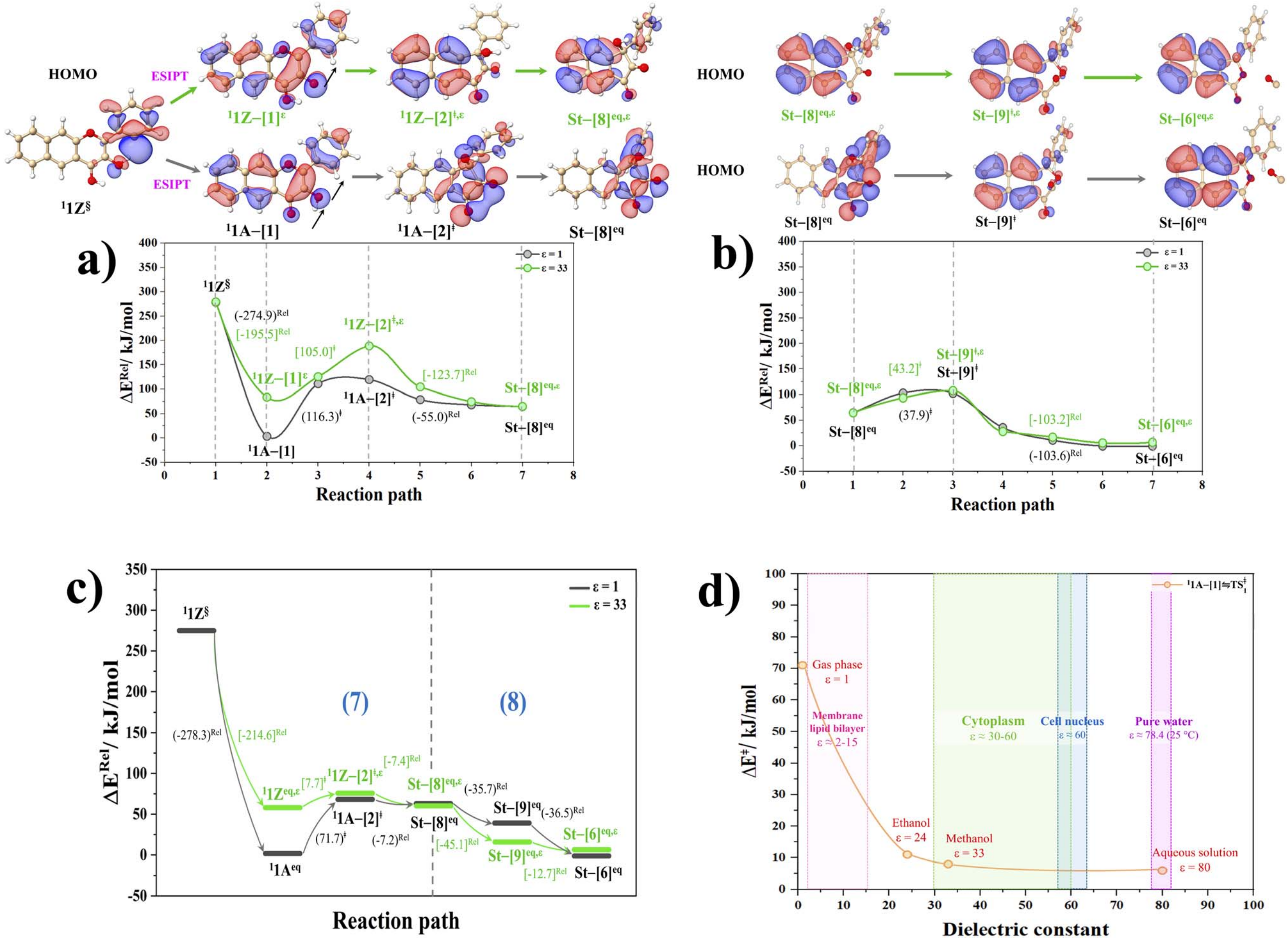

Fig. 6 (a and b) The S_0 PESs for formation of lactone and CO on the anaerobic pathway with $\varepsilon = 1$ and 33, E(**7**) and E(**8**) in Path (IV), respectively. (c) The S_0 potential energy profiles for formation lactone and CO on the anaerobic pathway [Path (IV)] computed with $\varepsilon = 1$ and 33. (d) Energy barrier ($\Delta E^{\ddagger}$) of the rate-determining step in the anaerobic pathway [E(**7**) in Path (IV)] as a function of the dielectric constant in the intracellular environment (ε = 1–80). The symbols used are explained in the text. ΔE^{Rel} = relative energy with respect to the precursor in the S_0 state in kJ mol^{-1}; $(\ldots)^{\mathrm{Rel}}$ and $(\ldots)^{\ddagger}$ = relaxation energy and energy barrier on PES; $[\ldots]$ = structure and energy with $\varepsilon = 33$, respectively; → = proton/hydrogen transfer direction.

profiles reveal the anaerobic pathway as the rate-determining reaction. Hence, our study focused only on Path (IV). Because the T_c for the elementary reactions are far below human body temperature, the quantum effects do not play important roles, and it is reasonable to use $k_{f/r}^{Q\text{-vib}}$ in the thermodynamic and kinetic analysis. All the kinetic and thermodynamic properties obtained from TST calculations are summarized in Tables S3–S7.

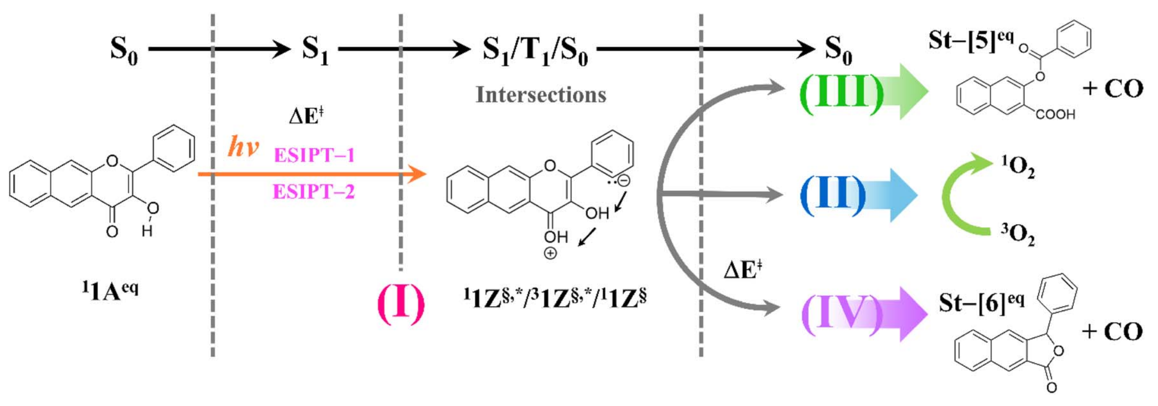

Fig. 7 Schematic representation of the aerobic and anaerobic pathways involved in the photodecarbonylation process, highlighting the double proton/hydrogen transfers in the S_1 state and the $S_1/T_1/S_0$ intersections.

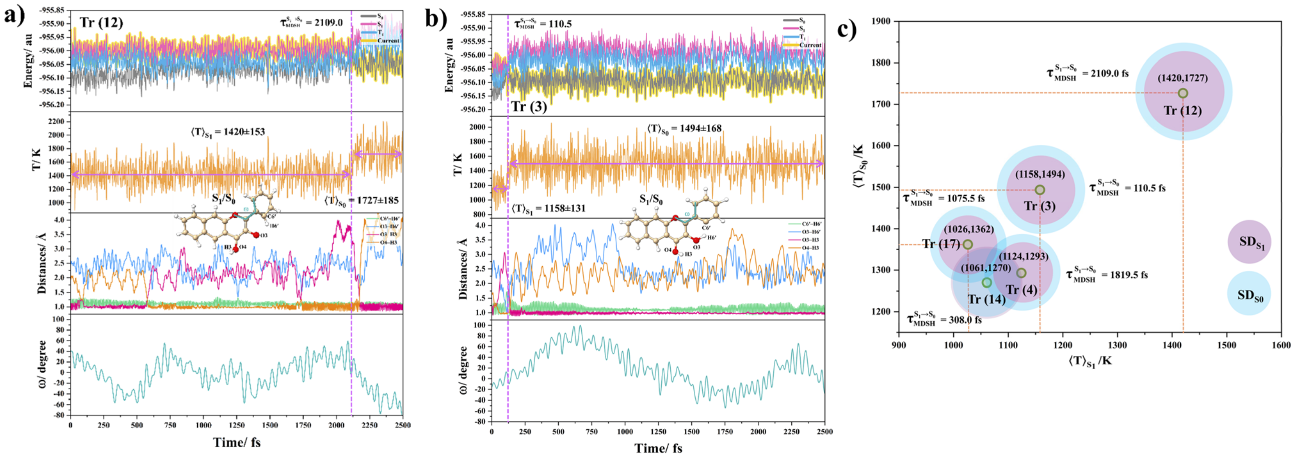

Fig. 8 (a and b) Examples of the time evolutions of the single and consecutive ESIPTs, obtained from NVE-MDSH simulations with $\varepsilon = 1$, respectively. (c) Correlation plot between the average temperatures in the S_1 and S_0 states for single and consecutive ESIPTs, obtained from NVE-MDSH simulations, $\tau_{MDSH}^{S_1\rightarrow S_0}$ = $S_1\rightarrow S_0$ surface hopping time; $\langle T\rangle_{S_1}$ = average temperature in the S_1 state; $\langle T\rangle_{S_0}$ = average temperature in the S_0 state; Tr (n) = NVE-MDSH trajectory number n.

For the aerobic pathway to generate salicylic acid ester and CO, the barrierless potential energy profiles (Fig. 5c), $k_{f/r}^{Q\text{-vib}}$ (Table S4), and total Gibbs free energies {$\Delta G^{\circ,\text{Tot,(III)}} = -615.6$ [-635.9] kJ mol^{-1} at 307 K (Table S7a)} confirm that E(**5**) and E(**6**) in Path (III) are kinetically and thermodynamically favorable. Whereas the energies (Fig. 6c), kinetic and thermodynamic properties (Tables S5 and S6) anticipate that E(**7**) and E(**8**) to generate lactone and CO *via* the anaerobic pathway in Path (IV) are considerably less favorable {$\Delta G^{\circ,\text{Tot,(IV)}} = -89.7$ [-178.5] kJ mol^{-1} at 307 K (Tables S7b and c)}. These results qualitatively support the experimental findings that the chemical yields obtained *via* the aerobic pathway are considerably higher than those obtained *via* the anaerobic pathway in methanol.[20]

The adiabatic potential energy profiles (Fig. 6c) suggest that E(7) *via* the anaerobic pathway [Path (IV)] is exclusively sensitive to the local dielectric environment and kinetically less favorable with $\varepsilon = 1$. This might be because E(7) with $\varepsilon = 1$ involves the acid form (^{1}**1A**$^{\mathbf{eq}}$), which is more stable than the basic form (^{1}**1Z**$^{\mathbf{eq},\varepsilon}$) with $\varepsilon = 33$. The highest Gibbs free energy barriers ($\Delta G^{\ddagger}$ = 70.5 [4.8] kJ mol^{-1}) in E(7) involves the six- to five-membered ring contraction {$k_{f}^{Q\text{-vib}} = 6.24 \times 10^{0}$ [1.29×10^{11}] s^{-1} at 307 K (Tables S5 and S6)}.

Surface hopping dynamics

To characterize the double ESIPTs, and estimate the $S_1 \rightarrow S_0$ surface hopping time ($\tau_{MDSH}^{S_1\rightarrow S_0}$), and nonradiative (vibrational) relaxation temperatures in E(**1**) and E(**2**), five representative NVE-MDSH trajectories with the surface hopping times of 110 fs $< \tau_{MDSH}^{S_1\rightarrow S_0} <$ 2109 fs were selected for the in-depth dynamic analysis. The S_1 potential energy profile with $\varepsilon = 33$ shows a considerably high $\Delta E^{\ddagger}$ for the second ESIPT (^{1}**1Z**$^{\ddagger,*,\varepsilon}$; Fig. S1b). Hence, the results with $\varepsilon = 1$ are emphasized. The time evolutions of the total energies of S_0, S_1, and T_1, characteristic H-bond distances, dihedral angle ω, and temperatures were plotted (Fig. S3). The characteristic results are summarized in Table S8 and two samples are presented in Fig. 8.

Analysis of the initial configurations (Table S8) reveals that the vertically excited structures inducing $S_1 \rightarrow S_0$ surface hopping exhibit $\Delta E^{S_0\rightarrow S_1}$ within a substantially narrow range [3.06–3.07 eV ($\lambda^{S_0\rightarrow S_1}$ = ∼404 nm)] with $\angle O_1\text{–}C_2\text{–}C_{1'}\text{–}C_{2'}$ (ω) varying in a wide range of $-17° < \omega < 39°$. The absorption wavelength ($\lambda^{S_0\rightarrow S_1}$) is in excellent agreement with the second outstanding peak obtained in the experiment (λ^{abs} = 401 nm).[20] The structures before and after $S_1 \rightarrow S_0$ nonradiative relaxation are dominated by single $O_3\text{–}H_3 \rightarrow O_4$ ESIPT (Fig. 8a). Among the five NVE-MDSH representatives (Fig. S3a–e), only one (Fig. 8b) exhibits consecutive ESIPTs. The low probability might arise (i) from the presence of $\Delta E^{\ddagger}$ = 23.0 kJ mol^{-1} preceding the second ESIPT (Fig. 4) and (ii) geometrical constraints, where coplanarity of $O_3\text{–}H_3\cdots O_4$ and $C_{6'}\text{–}H_{6'}\cdots O_3$ H-bonds is likely a prerequisite for the occurrence of the second ESIPT (^{1}**1Z**‡,* with $\omega = 0°$).

Dynamic analyses generally show higher average deactivation temperatures in S_0 than in S_1 (Fig. S3a–e). Because the second ESIPT is anticipated by the PESs to be the key step for the successive aerobic and anaerobic pathways, to assess the factors promoting the second ESIPT, the correlation between the average temperatures in S_1 and S_0 states was plotted. The correlation plot presented in Fig. 8c shows that for the second ESIPT, the ultrafast $\tau_{MDSH}^{S_1\rightarrow S_0}$ of 110 fs (Fig. 8b) reflects correlations between the average temperature in S_1 ($\langle T\rangle_{S_1}$) and S_0 ($\langle T\rangle_{S_0}$) of 1158 ± 131 K and 1494 ± 168 K, respectively, implying that the kinetic energies in the S_1 ($\langle \text{KE}\rangle_{S_1}$) and S_0 ($\langle \text{KE}\rangle_{S_0}$) states of 466 ± 53 and 600 ± 65 kJ mol^{-1}, respectively (Table S8), cooperatively facilitate the second ESIPT. Thus, the second ESIPT arises from the synergistic effect of vibrational relaxations in the S_1 and S_0 states.

It is worth noting the exothermic photo-to-thermal energy observed in the S_0 state. Because thermal energy is by-product of E(**1**) and E(**2**), the integration of photothermal therapy (PTT) into PDT appears feasible. PTT generally uses nanoparticles or photosensitizers that convert NIR light into heat, increasing local temperature to kill cancer/tumor cells. Herein, luminal A breast adenocarcinoma or MCF-7 (Michigan Cancer Foundation-7), a standard breast cancer cell model, was used as an example. Because thermal necrosis (irreversible cell and tissue death caused by excessive heat) requires intracellular temperature in the range of T = 315–333 K[50] and the average volume of MCF-7 is $V_{\text{MCF-7}} = 1.76 \times 10^{-12}$ L,[51] the thermal energy requires to increase the intracellular temperature from T = 310 (human body temperature) to 333 K (ΔT = 23 K) could be calculated from the thermal energy released from the photo-to-thermal process; for example, for the photoexcited Flavonol-1 in Fig. 8b, $\langle T \rangle_{S_0} = 1494 \pm 168$ K and $\langle \text{KE} \rangle_{S_0} = 600 \pm 65$ kJ mol^{-1} (Table S8).

Assuming that 80% of the MCF-7 cell volume is cytosolic liquid (or liquid water),[52] $V_{H_2O} = 1.41 \times 10^{-9}$ cm^3, $m_{H_2O} = 1.41 \times 10^{-9}$ g and $s_{H_2O} = 4.184$ J (g K)$^{-1}$, and $Q_{H_2O} = m_{H_2O}s_{H_2O}\Delta T = 1.35 \times 10^{-7}$ J. Therefore, the amount of Flavonol-1 (photosensitizer) required to increase the intracellular temperature of a single MCF-7 cell is 2.26×10^{-13} mol. The calculated value is reasonable compared with the average intracellular concentration of doxorubicin (a widely used chemotherapy drug used to treat breast cancer and others) in MCF-7 cells, approximately 0.5–1 μM after 168 hours of the cellular exposure,[53] corresponding to 7.5×10^{-19}–1.41×10^{-18} mol in the same cytosolic liquid volume (1.41×10^{-9} cm^3). These theoretical findings indicate that Flavonol-1 may possess characteristics consistent with a potential photosensitizer capable of contributing to both PDT and PTT processes.

Conclusion

PDT, a promising medical treatment for various human diseases, is effective based on the efficiency of the photosensitizer to transfer photon energy to target molecules. The intrinsic toxicity of CO can have therapeutic applications in cancer treatment. Hence, photoCORMs represent a new technology for releasing and managing CO in cancer cells *via* photochemical reactions, controlling CO release in the target location and timing.

Herein, complementary theoretical approaches were used to systematically investigate the elementary reactions involved in the proposed photodecarbonylation mechanism of Flavonol-1, an organic photoCORM. To examine the mechanisms under low (ε = 1; gas phase) and high (ε = 33; methanol) dielectric environments, DFT and TD-DFT/B3LYP/def2-TZVP methods were rigorously tested. The reliability of these methods was confirmed by successfully benchmarking against all reported theoretical and experimental photophysical properties.

The proposed photodecarbonylation mechanism was delineated into four pathways, encompassing eight elementary reactions under aerobic and anaerobic conditions: (i) E(**1**) and E(**2**) are photoexcitation and acid–base reactions to generate an intermediate in the triplet state [^{3}**1Z*** in Path (I)], (ii) E(**3**)–E(**6**) are the aerobic pathways [Paths (II) and (III)], and (iii) E(**7**) and E(**8**) are the anaerobic pathway [Path (IV)]. Because the singlet → triplet excitation is spin forbidden, the photoexcitation and acid–base reactions [Path (I)] were primarily assumed to occur in the lowest singlet excited electronic state.

The S_1 PESs obtained from TD-DFT/B3LYP/def2-TZVP calculations showed for the first time that $S_0 \rightarrow S_1$ vertical excitation and librational motion of ω promoted the acid–base reaction with two consecutive ESIPTs. The second ESIPT induced S_1/T_1 and T_1/S_0 electronic state intersections. The S_1 PES with $\varepsilon = 1$ exhibited low $\Delta E^{\ddagger}$. Hence, the acid–base reaction (the O_3–$H_3 \rightarrow O_4$ proton/hydrogen transfer) along Path (I) was likely favored in nonpolar solvents. In contrast, when ε = 33, owing to high $\Delta E^{\ddagger}$ for the second ESIPT (the $C_{6'}$–$H_{6'} \rightarrow O_3$ proton/hydrogen transfer), the $S_1 \rightarrow S_0$ fluorescence of the basic form of Flavonol-1 is highly favorable, which is supported by the intense fluorescence band of the basic form observed *via* nanosecond time-resolved spectroscopy.

Based on the hypothesis that the structures at the S_1/T_1, S_1/S_0 and T_1/S_0 electronic state intersections are reactive precursors for successive aerobic and anaerobic pathways in the S_0 state, several low $\Delta E^{\ddagger}$ deactivation processes were observed. The S_1/T_1 ISC rate is fast, whereas the $T_1 \rightarrow S_0$ (phosphorescence) rate is slow, with the energy release comparable with the energy required for $^3O_2 \rightarrow {}^1O_2$. Hence, formation of the singlet oxygen proceeds favorably *via* E(**1**) → E(**4**) [Path (I) and (II)].

For the photodecarbonylation along the aerobic pathway [Path (III)], analysis of S_0 PESs revealed that formation of salicylic acid ester and CO from the intersection structures proceeded without $\Delta E^{\ddagger}$, rendering the process thermodynamically and kinetically favorable. In contrast, along the anaerobic pathway forming lactone and CO [Path (IV)], the elementary reaction involving the contraction of the six-membered ring to a five-membered ring exhibited high $\Delta E^{\ddagger}$ in the gas phase (ε = 1) but low $\Delta E^{\ddagger}$ in the intracellular dielectric environment (ε = 30–60). Together with the kinetic and thermodynamic analyses, these findings qualitatively support the experimental observation that chemical yields in the aerobic pathway are higher than those in the anaerobic pathway.

To investigate the characteristic dynamics of ESIPTs and assess the potential of Flavonol-1 for dual-mode phototherapy integrating PDT and PTT, the photo-to-thermal conversion was estimated from NVE-MDSH results. The thermal analysis suggested that irradiation of 2.26×10^{-13} mol of Flavonol-1 could increase the cytosolic liquid temperature in an MCF-7 cell to 333 K, corresponding to the local temperature required for thermal necrosis. Because efficient photosensitizer delivery to target cells is a key determinant of PDT and PTT efficacy, our forthcoming theoretical study will investigate the photodynamic behavior of Flavonol-1 embedded within a specific nanostructure. The outcomes will provide a basis for future theoretical and experimental efforts aimed at optimizing or designing highly effective PDT/PTT photosensitizers.

Author contributions

Promma: methodology; data curation; formal analysis; investigation; software. Lao-Ngam: investigation; formal analysis. Panajapo: methodology; data curation; formal analysis;

investigation; software. Photiganit: methodology; data curation; formal analysis; investigation; software; validation; visualization. Thongyu: methodology; data curation; formal analysis; investigation; software; validation; visualization. Sagarik: funding acquisition, supervision; project administration; conceptualization; writing – original draft; writing – review & editing.

Conflicts of interest

There are no conflicts of interest to declare.

Data availability

The data supporting this article have been included as part of the supplementary information (SI). Supplementary information: the S_0, S_1 and T_1 PESs for the elementary reactions [E(**1**)–E(**4**); Path (I)–(II)] with $\varepsilon = 33$; the S_0 PESs for elementary reactions [E(**7**)–E(**8**); Path (IV)] with ε = 1–80; time-evolution of single and consecutive ESIPTS [E(**1**)–E(**2**); Path (I)], obtained from NVE-MDSH with $\varepsilon = 1$; all equilibrium and characteristic structures on the S_0, S_1 and T_1 PESs obtained from DFT and TD-DFT/B3LYP/def2-TZVP methods with $\varepsilon = 1$ and 33; all the thermodynamic and kinetic properties for all the elementary reactions with $\varepsilon = 1$ and 33, obtained from the TST method; all the characteristic dynamic results in the S_1 and S_0 states obtained from NVE-MDSH with $\varepsilon = 1$. See DOI: **https://doi.org/10.1039/d5ra07859h**.

Acknowledgements

This work was financially supported by Suranaree University of Technology (Grant Number: IRD1-102-68-12-14).

References

1 A. Hak, V. R. Shinde and A. K. Rengan, A review of advanced nanoformulations in phototherapy for cancer therapeutics, *Photodiagn. Photodyn. Ther.*, 2021, **33**, 102205.

2 J. Piskorz, W. Porolnik, M. Kucinska, J. Dlugaszewska, M. Murias and J. Mielcarek, BODIPY-based photosensitizers as potential anticancer and antibacterial agents: role of the positive charge and the heavy atom effect, *ChemMedChem*, 2021, **16**, 399–411.

3 Y. Zhang, Z. Yang, X. Zheng, L. Yang, N. Song, L. Zhang, L. Chen and Z. Xie, Heavy atom substituted near-infrared BODIPY nanoparticles for photodynamic therapy, *Dyes Pigm.*, 2020, **178**, 108348.

4 A. Escudero, C. Carrillo-Carrión, M. C. Castillejos, E. Romero-Ben, C. Rosales-Barrios and N. Khiar, Photodynamic therapy: photosensitizers and nanostructures, *Mater. Chem. Front.*, 2021, **5**, 3788–3812.

5 X. F. Zhang, X. Yang, K. Niu and H. Geng, Phosphorescence of BODIPY dyes, *J. Photochem. Photobiol., A*, 2014, **285**, 16–20.

6 M. J. Davies, Singlet oxygen-mediated damage to proteins and its consequences, *Biochem. Biophys. Res. Commun.*, 2003, **305**, 761–770.

7 S. N. Anderson, M. T. Larson and L. M. Berreau, Solution or solid–it doesn't matter: visible light-induced CO release reactivity of zinc flavonolato complexes, *Dalton Trans.*, 2016, **45**, 14570–14580.

8 S. H. Heinemann, T. Hoshi, M. Westerhausen and A. Schiller, Carbon monoxide– physiology, detection and controlled release, *Chem. Commun.*, 2014, **50**, 3644–3660.

9 E. Üstün, M. C. Ayvaz, M. S. Çelebi, G. Aşçı, S. Demir and İ. Özdemir, Structure, CO-releasing property, electrochemistry, DFT calculation, and antioxidant activity of benzimidazole derivative substituted $[Mn(CO)_3(bpy)L]PF_6$ type novel manganese complexes, *Inorg. Chim. Acta*, 2016, **450**, 182–189.

10 B. Wegiel, D. Gallo, E. Csizmadia, C. Harris, J. Belcher, G. M. Vercellotti, N. Penacho, P. Seth, V. Sukhatme and A. Ahmed, Carbon monoxide expedites metabolic exhaustion to inhibit tumor growth, *Cancer Res.*, 2013, **73**, 7009–7021.

11 V. Yempally, S. J. Kyran, R. K. Raju, W. Y. Fan, E. N. Brothers, D. J. Darensbourg and A. A. Bengali, Thermal and photochemical reactivity of manganese tricarbonyl and tetracarbonyl complexes with a bulky diazabutadiene ligand, *Inorg. Chem.*, 2014, **53**, 4081–4088.

12 H. M. Southam, T. W. Smith, R. L. Lyon, C. Liao, C. R. Trevitt, L. A. Middlemiss, F. L. Cox, J. A. Chapman, S. F. El-Khamisy and M. Hippler, A thiol-reactive Ru(II) ion, not CO release, underlies the potent antimicrobial and cytotoxic properties of CO-releasing molecule-3, *Redox Biol.*, 2018, **18**, 114–123.

13 M. Martínek, L. Filipová, J. Galeta, L. Ludvíková and P. Klán, Photochemical formation of dibenzosilacyclohept-4-yne for Cu-free click chemistry with azides and 1,2,4,5-tetrazines, *Org. Lett.*, 2016, **18**, 4892–4895.

14 G. Kuzmanich and M. A. Garcia-Garibay, Ring strain release as a strategy to enable the singlet state photodecarbonylation of crystalline 1, 4-cyclobutanediones, *J. Phys. Org. Chem.*, 2011, **24**, 883–888.

15 O. Chapman, P. Wojtkowski, W. Adam, O. Rodriguez and R. Rucktäschel, Photochemical transformations. XLIV. Cyclic peroxides synthesis and chemistry of alpha-lactones, *J. Am. Chem. Soc.*, 1972, **94**, 1365–1367.

16 P. Peng, C. Wang, Z. Shi, V. K. Johns, L. Ma, J. Oyer, A. Copik, R. Igarashi and Y. Liao, Visible-light activatable organic CO-releasing molecules (PhotoCORMs) that simultaneously generate fluorophores, *Org. Biomol. Chem.*, 2013, **11**, 6671–6674.

17 L. A. Antony, T. Slanina, P. Sebej, T. Solomek and P. Klan, Fluorescein analogue xanthene-9-carboxylic acid: a transition-metal-free CO releasing molecule activated by green light, *Org. Lett.*, 2013, **15**, 4552–4555.

18 T. Solomek, J. Wirz and P. Klan, Searching for improved photoreleasing abilities of organic molecules, *Acc. Chem. Res.*, 2015, **48**, 3064–3072.

19 K. Grubel, B. J. Laughlin, T. R. Maltais, R. C. Smith, A. M. Arif and L. M. Berreau, Photochemically-induced dioxygenase-type CO-release reactivity of group 12 metal flavonolate complexes, *Chem. Commun.*, 2011, **47**, 10431–10433.

20 M. Russo, P. Stacko, D. Nachtigallová and P. Klán, Mechanisms of orthogonal photodecarbonylation reactions of 3-hydroxyflavone-based acid–base forms, *J. Org. Chem.*, 2020, **85**, 3527–3537.

21 P. K. Mandal and A. Samanta, Evidence of ground-state proton-transfer reaction of 3-hydroxyflavone in neutral alcoholic solvents, *J. Phys. Chem. A*, 2003, **107**, 6334–6339.

22 M. J. Colín, M. Á. Aguilar and M. E. Martín, A theoretical study of solvent effects on the structure and UV–Vis spectroscopy of 3-hydroxyflavone (3-hf) and some simplified molecular models, *ACS Omega*, 2023, **8**, 19939–19949.

23 P. K. Sengupta and M. Kasha, Excited state proton-transfer spectroscopy of 3-hydroxyflavone and quercetin, *Chem. Phys. Lett.*, 1979, **68**, 382–385.

24 M. L. Martinez, S. L. Studer and P. T. Chou, Direct evidence of the triplet-state origin of the slow reverse proton transfer reaction of 3-hydroxyflavone, *J. Am. Chem. Soc.*, 1990, **112**, 2427–2429.

25 T. Matsuura, H. Matsushima and R. Nakashima, Photoinduced reactions—XXXVI: photosensitized oxygenation of 3-hydroxyflavones as a nonenzymatic model for quercetinase, *Tetrahedron*, 1970, **26**, 435–443.

26 T. Matsuura, H. Matsushima and H. Sakamoto, Photosensitized oxygenation of 3-hydroxyflavones possible model for biological oxygenation, *J. Am. Chem. Soc.*, 1967, **89**, 6370–6371.

27 T. Matsuura, T. Takemoto and R. Nakashima, Photoinduced reactions—LXXI: photorearrangement of 3-hydroxyflavones to 3-aryl-3-hydroxy-1,2-indandiones, *Tetrahedron*, 1973, **29**, 3337–3340.

28 T. Khrootkaew, S. Wangngae, K. Chansaenpak, K. Rueantong, W. Wattanathana, P. Pinyou, P. Panajapo, V. Promarak, K. Sagarik and A. Kamkaew, Heavy atom effect on the intersystem crossing of a boron difluoride formazanate complex-based photosensitizer: experimental and theoretical studies, *Chem.–Asian J.*, 2024, **19**, e202300808.

29 P. Suwannakham, P. Panajapo, P. Promma, T. Khrootkaew, A. Kamkaew and K. Sagarik, Photoluminescence mechanisms of BF_2-formazanate dye sensitizers: a theoretical study, *RSC Adv.*, 2024, **14**, 20081–20092.

30 S. G. Balasubramani, G. P. Chen, S. Coriani, M. Diedenhofen, M. S. Frank, Y. J. Franzke, F. Furche, R. Grotjahn, M. E. Harding, C. Hattig, A. Hellweg, B. Helmich-Paris, C. Holzer, U. Huniar, M. Kaupp, A. Marefat Khah, S. Karbalaei Khani, T. Muller, F. Mack, B. D. Nguyen, S. M. Parker, E. Perlt, D. Rappoport, K. Reiter, S. Roy, M. Ruckert, G. Schmitz, M. Sierka, E. Tapavicza, D. P. Tew, C. van Wullen, V. K. Voora, F. Weigend, A. Wodynski and J. M. Yu, TURBOMOLE: modular program suite for *ab initio* quantum-chemical and condensed-matter simulations, *J. Chem. Phys.*, 2020, **152**, 184107.

31 E. Tapavicza, I. Tavernelli, U. Rothlisberger, C. Filippi and M. E. Casida, Mixed time-dependent density-functional theory/classical trajectory surface hopping study of oxirane photochemistry, *J. Chem. Phys.*, 2008, **129**, 124108.

32 J. Nirasok, P. Panajapo, P. Promma, P. Suwannakham and K. Sagarik, Dynamics and mechanisms of nonradiative photodissociation of glycine: A theoretical study, *J. Photochem. Photobiol., A*, 2023, **436**, 114354.

33 P. Panajapo, P. Suwannakham, P. Promma and K. Sagarik, Mechanisms of glycine formation in cold interstellar media: a theoretical study, *R. Soc. Open Sci.*, 2024, **11**, 231957.

34 M. W. Baig, M. Pederzoli, M. Kývala, L. Cwiklik and J. Pittner, Theoretical investigation of the effect of alkylation and bromination on intersystem crossing in BODIPY-based photosensitizers, *J. Phys. Chem. B*, 2021, **125**, 11617–11627.

35 A. Klamt, V. Jonas, T. Bürger and J. C. W. Lohrenz, Refinement and parametrization of COSMO-RS, *J. Phys. Chem. A*, 1998, **102**, 5074–5085.

36 A. Klamt and G. Schüürmann, COSMO: a new approach to dielectric screening in solvents with explicit expressions for the screening energy and its gradient, *J. Chem. Soc., Perkin Trans. 2*, 1993, 799–805.

37 T. A. Halgren and W. N. Lipscomb, The synchronous-transit method for determining reaction pathways and locating molecular transition states, *Chem. Phys. Lett.*, 1977, **49**, 225–232.

38 P. Plessow, Reaction path optimization without NEB springs or interpolation algorithms, *J. Chem. Theory Comput.*, 2013, **9**, 1305–1310.

39 F. Neese, The ORCA program system, *Comput. Mol. Biosci.*, 2012, **2**, 73–78.

40 F. Neese, The ORCA quantum chemistry program package, *Comput. Mol. Biosci.*, 2022, **12**, e1606.

41 J. E. House, *Principles of Chemical Kinetics, Kindle Edition*, Academic Press, USA, 2nd edn, 2007.

42 E. Wigner, The transition state method, *J. Chem. Soc., Faraday Trans.*, 1938, **32**, 29.

43 E. Wigner, On the crossing of potential thresholds in chemical reactions, *Z. Phys. Chem.*, 1932, **15**, 203.

44 J. Kästner, J. M. Carr, T. W. Keal, W. Thiel, A. Wander and P. Sherwood, DL-FIND: an open-source geometry optimizer for atomistic simulations, *J. Phys. Chem. A*, 2009, **113**, 11856–11865.

45 ChemShell, a Computational Chemistry Shell, **http://www.chemshell.org**.

46 M. Barbatti, M. Ruckenbauer, F. Plasser, J. Pittner, G. Granucci, M. Persico and H. Lischka, Newton-X: a surface-hopping program for nonadiabatic molecular dynamics, *Wiley Interdiscip. Rev.: Comput. Mol. Sci.*, 2014, **4**, 26–33.

47 G. A. Brucker and D. F. Kelley, Proton transfer in matrix-isolated 3-hydroxyflavone and 3-hydroxyflavone complexes, *J. Phys. Chem.*, 1987, **91**, 2856–2861.

48 S. L. Studer, W. E. Brewer, M. L. Martinez and P. T. Chou, Time-resolved study of the photooxygenation of 3-hydroxyflavone, *J. Am. Chem. Soc.*, 1989, **111**, 7643–7644.

49 W. Wang, K. Foley, X. Shan, S. Wang, S. Eaton, V. J. Nagaraj, P. Wiktor, U. Patel and N. Tao, Single cells and intracellular

processes studied by a plasmonic-based electrochemical impedance microscopy, *Nat. Chem.*, 2011, **3**, 249–255.

50 Z. Xie, T. Fan, J. An, W. Choi, Y. Duo, Y. Ge, B. Zhang, G. Nie, N. Xie, T. Zheng, Y. Chen, H. Zhang and J. S. Kim, Emerging combination strategies with phototherapy in cancer nanomedicine, *Chem. Soc. Rev.*, 2020, **49**, 8065–8087.

51 M. P. Gamcsik, K. K. Millis and O. M. Colvin, Noninvasive detection of elevated glutathione levels in MCF-7 cells resistant to 4-hydroperoxycyclophosphamide, *Cancer Res.*, 1995, **55**, 2012–2016.

52 F. Nolin, J. Michel, L. Wortham, P. Tchelidze, G. Balossier, V. Banchet, H. Bobichon, N. Lalun, C. Terryn and D. Ploton, Changes to cellular water and element content induced by nucleolar stress: investigation by a cryo-correlative nano-imaging approach, *Cell. Mol. Life Sci.*, 2013, **70**, 2383–2394.

53 S.-H. Tsou, T.-M. Chen, H.-T. Hsiao and Y.-H. Chen, A critical dose of doxorubicin is required to alter the gene expression profiles in MCF-7 cells acquiring multidrug resistance, *PLoS One*, 2015, **10**, e0116747.